Arch. Metall. Mater. **71** (2026), 3, 873-881

DOI: https://doi.org/10.24425/amm.2026.1979

TOMASZ GORYCZKA[1], WOJCIECH MAZIARZ[2], ZBIGNIEW STOKŁOSA[1],
MACIEJ ZUBKO[1] PATRICK OCHIN[3]

EFFECT OF VIBRATION MILLING TIME ON STRUCTURE, CHEMICAL COMPOSITION AND FRAGMENTATION–AGGLOMERATION PROCESSES IN POWDERS PRODUCED FROM MELT-SPUN Ni–Mn–Ga RIBBONS

Ni–Mn–Ga alloy ribbons were produced by melt spinning and subsequently processed by vibration milling for 15, 30, 60 and 240 minutes. The influence of milling time on chemical composition, phase structure and microstructural parameters was investigated using laser diffraction, scanning electron microscopy (SEM) and X-ray diffraction (XRD). Chemical analysis revealed a gradual decrease in Ga content accompanied by a relative increase in Ni and Mn, leading to a systematic increase in the valence electron concentration (*e*/*a*). XRD results showed a milling-time-dependent transition from the ordered $L2_1$ structure in the as-spun ribbon to 14M martensite in the milled powders. Particle size analysis indicated a reduction in characteristic particle diameters with milling time, along with the formation of a secondary fine fraction originating from the ribbon microstructure. Williamson-Hall analysis revealed a decrease in crystallite size and an increase in microstrain in the parent phase. In contrast, the martensite exhibited finer, more uniform crystallite sizes and relatively low microstrain.

Keywords: Ni–Mn–Ga alloys; vibration milling; order-disorder; martensite 14M; microstrain; crystallite size

1. Introduction

Ni–Mn–Ga alloys belong to the wide group of ferromagnetic shape memory alloys (FSMA). Their unique functional properties have attracted considerable interest since their discovery. Particular attention has been paid to magnetic-field-induced strain (MFIS). This effect is directly associated with the martensitic transformation occurring in the ferromagnetic state and is related to the reorientation of martensite variants [1]. The largest strains, reaching several to over 10%, have been observed in single crystals. However, in polycrystalline materials, this effect is significantly reduced. It is due to the presence of grain boundaries, which hinder twin boundary motion [2,3].

It is well established that the properties of shape memory alloys, both conventional and magnetic, can be modified by changes in chemical composition and/or structure [4]. For this purpose, small additions of alloying elements such as Fe, Co, or rare earth elements (e.g., Nd, Sm, Tb) have been introduced into Ni–Mn–Ga alloys. These modifications improve mechanical properties, although often at the expense of magnetic performance [5,6]. An alternative approach to tailoring the properties of these alloys involves microstructural modification through plastic deformation and/or thermomechanical treatment. However, in the case of Ni–Mn–Ga alloys, such processing routes are strongly limited by their inherent brittleness. Therefore, efforts have been made to produce materials in their final form, particularly as thin ribbons with controlled microstructure and texture. One of the commonly applied techniques is melt spinning, which enables the production of ribbons with pronounced crystallographic texture and a columnar grain. This structure results from directional solidification under high thermal gradients. Such materials constitute an interesting alternative to conventional polycrystalline alloys [7-10].

The high brittleness of Ni–Mn–Ga alloys, while limiting their processing and bulk applications can also be considered advantageous for comminution, enabling efficient mechanical powder production. Consequently, extensive research has been devoted to the preparation of Ni–Mn–Ga powders, which are used, among others, in functional composites. Various processing routes have been employed, including ball milling (planetary and vibratory), spark erosion, and atomisation [11-14]. In most cases, powders have been produced directly from bulk materials.

[1] UNIVERSITY OF SILESIA IN KATOWICE, INSTITUTE OF MATERIALS ENGINEERING, 75 PUŁKU 1A, 41-500 CHORZÓW, POLAND
[2] INSTITUTE OF METALLURGY AND MATERIALS SCIENCE, POLISH ACADEMY OF SCIENCES,25 REYMONTA STR., 30-059 KRAKOW, POLAND
[3] INSTITUT DE CHIMIE ET DES MATÉRIAUX PARIS-EST, CNRS, PARIS, FRANCE

* Corresponding author: tomasz.goryczka@us.edu.pl

In the present work, a different approach to powder preparation was applied. In the first stage, ribbons were produced by melt spinning and subsequently subjected to mechanical milling. This approach makes it possible to utilize the specific microstructure of the initial material, particularly its texture and gradient structure, which may influence the fragmentation mechanism during milling. It can be utilised and may influence the fragmentation mechanism. The main objective of this study was to analyse the effect of milling time on the degree of material refinement and particle size distribution, as well as to identify the processes responsible for the formation of powders with varied morphology and microstructure. In addition, the effect of milling time on the material's chemical composition and phase constitution was investigated.

2. Experimental procedure

2.1. Material

A Ni–Mn–Ga alloy with a nominal composition of Ni 51.5 at.%, Mn 27.5 at.%, and Ga 21.0 at.% was prepared from commercially available elements of technical purity. Melting was carried out in an induction furnace under a protective argon atmosphere. For the subsequent stage, i.e., ribbon production, ingots were zone-remelted into a rod-like form. This material was used directly as feedstock for the rapid solidification process.

In the melt-spinning process, the molten alloy was ejected onto the surface of a rotating wheel under 0.15 MPa of argon pressure. The melt temperature was 1250 °C, and the peripheral speed of the wheel was 19 m/s. Due to the high brittleness of the material, fragmentation of the solidified ribbon occurred during its ejection from the wheel surface. As a result, ribbon fragments with lengths ranging from approximately 5 mm to 30 mm were obtained. The average thickness was determined from microscope observations of cross-sectional images. Measurements were performed on five independent fracture surfaces, yielding a value of 28 ± 3 μm. The observed thickness variation is typical for melt-spun ribbons and results from the free-surface topography.

Finally, the powders were produced by mechanical milling of ribbon fragments using a vibratory mill (Fritsch PULVERISETTE 0). The process was carried out with a single 50 mm tungsten carbide (WC) milling ball and vibration amplitude of 0.5 mm. Four separate batches of ribbon fragments, each weighing about 10 g, were prepared for milling times of 15, 30, 60, and 240 min, respectively. This batch mass resulted in a ball-to-powder mass ratio of approximately 95:1. To limit heating of the charge during milling, a 30 min pause was introduced after each 60 min milling interval.

2.2. Experimental methods

Particle size characterisation was performed using laser diffraction. Measurements of particle size distributions for powders obtained after different milling times were done using a laser particle size analyser, Analysette 22 NeXT (Fritsch). The instrument allows analyses of particles in the range from approximately 0.01 μm to 3800 μm. Measurements were conducted in a wet dispersion mode. Based on the obtained results, the powders were characterised using the following parameters: volume-weighted mean diameter D(4,3), emphasising the contribution of larger particles; median diameter (D50), corresponding to the value below which 50% of the particle volume is contained; mode –representing the maximum of the distribution; arithmetic mean particle diameter; standard deviation (σ) – as a measure of data dispersion; and coefficient of variation (CV) – defined as the ratio of the standard deviation to the mean value.

Microstructure and morphology were examined using scanning electron microscopy (SEM). Both the surfaces and fracture cross-sections of the ribbons, as well as the morphology of particles after milling, were analysed. The investigations were carried out using a JSM-7100F TTL LV microscope (Jeol Ltd., Tokyo, Japan), equipped with a field emission gun (FEG) and an energy-dispersive X-ray spectroscopy (EDS) detector. SEM observations and chemical composition measurements were performed at an accelerating voltage of 20 kV.

The phase composition of the ribbons (initial material) and the powders after milling was studied from X-ray diffraction patterns. Measurements were done using an X'Pert-PRO diffractometer equipped with a CuKα radiation source ($\lambda K\alpha_1$ = 1.5406 Å, $\lambda K\alpha_2$ = 1.5445 Å). Diffraction patterns were measured over a 2θ range of 15° to 140° in step-scan mode with a step size of 0.04° (2θ). The counting time was adjusted individually to ensure comparable counting statistics. To evaluate the effect of milling time on crystallite size, the measured diffraction patterns were fitted using the Le Bail method implemented in Rietica software (version 4.2) [15]. Crystallographic data used for modelling the unit cells of the parent $L2_1$ phase were taken from the ICDD PDF database (card no. 03-065-0618). Structural parameters of the 14M martensite phase were adopted from the literature [16]. Crystallite size and lattice strain were determined from the full width at half maximum (FWHM) of diffraction peaks using the Williamson-Hall method [17].

3. Results and discussion

3.1. Microstructure and morphology

During melt spinning, ribbons with two characteristic surfaces were produced, revealing significant morphological differences under different heat-dissipation conditions. The SEM images shown in Fig. 1a and 1b present different fragments of the ribbon, including both the free surface (FS) and the transverse fracture (Fr). It should be emphasised that both images show the ribbon's free surface. However, they were taken from different regions across its width. Therefore, the observed differences concern both the local morphology of the free surface and the microstructure visible in the fracture surface. A well-developed,

fine-dispersed globular structure characterises the free surface shown in the upper part of Fig. 1a. This structure consists of numerous hemispherical protrusions of similar size. These features are related to the surface morphology formed during the rapid solidification of the ribbon. In contrast, Fig. 1b shows another fragment of the ribbon free surface, located closer to its edge. In this region, the surface is much flatter and lacks the distinct protrusions observed in Fig. 1a. These differences indicate local heterogeneity in the free-surface morphology, resulting from variations in liquid-metal flow and solidification conditions across different regions of the ribbon width.

At the same time, a microstructural gradient through the ribbon thickness is visible in the transverse fracture. In the region closer to the free surface, a transition from the near-surface globular region to the internal columnar structure can be observed. The columnar structure consists of elongated grains growing approximately perpendicular to the ribbon surface. The grains revealed a parallel arrangement and a high aspect ratio, indicating the directional nature of the solidification process under a high-temperature gradient. In the part of the cross-section corresponding to the wheel-contact side, the microstructure becomes more irregular. Flat fracture surfaces and local deformation features are visible, indicating a transcrystalline fracture mode. The observed structural gradient is a direct result of differences in heat extraction during melt spinning. Differences in cooling rate between the free surface and the wheel-contact side result in a heterogeneous morphology. It may play an important role in the milling fragmentation mechanism.

The effect of milling time on powder morphology and microstructure is shown in Fig. 1c-f. After 15 minutes of milling (Fig. 1c), intensive fragmentation of the ribbon was observed, leading to the formation of irregular particles, often plate-like

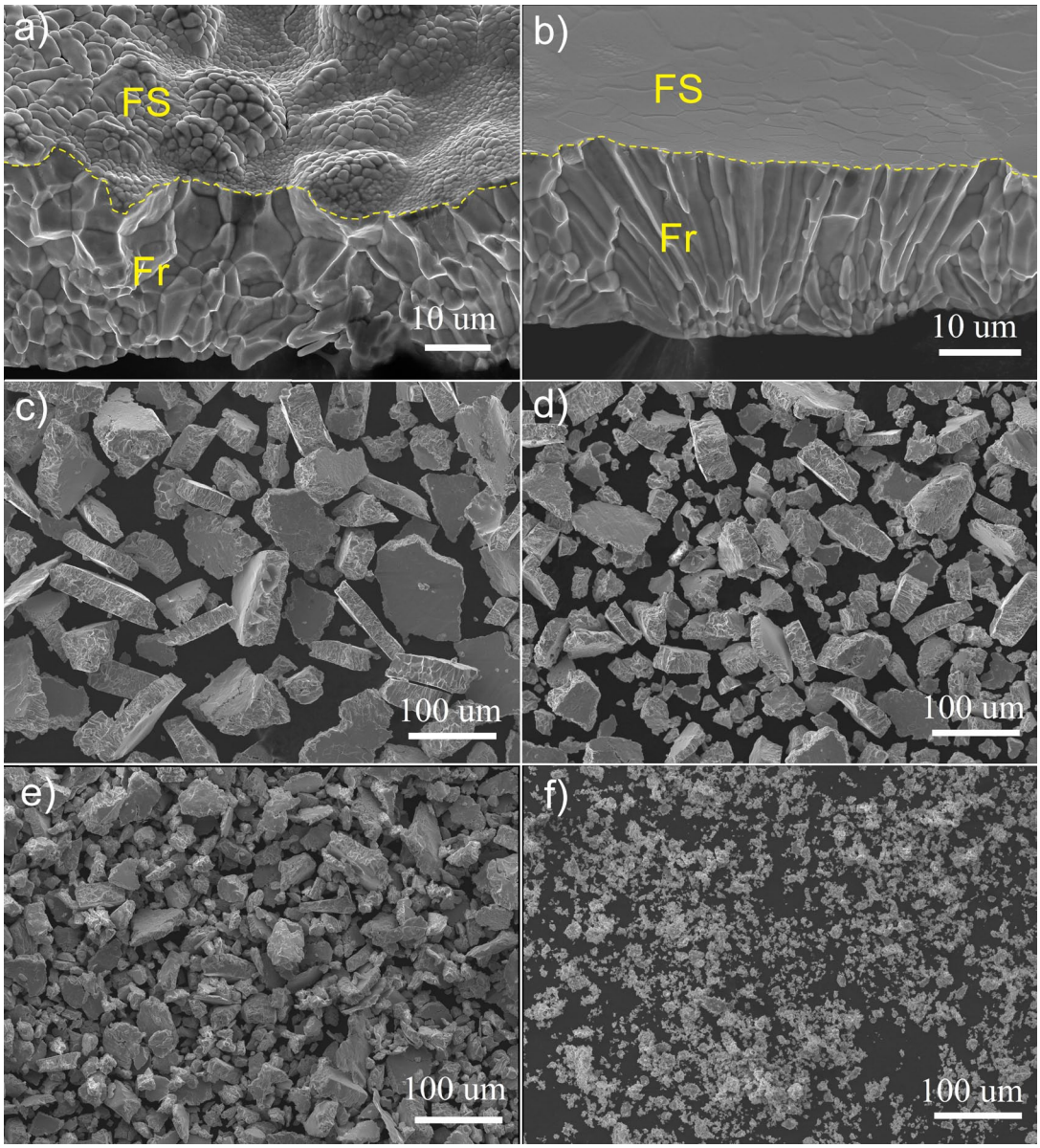

Fig. 1. SEM micrographs of the melt-spun ribbon and powders after milling: ribbon fragments showing the free surface (FS) and fracture surface (Fr) in regions with globular surface morphology (a) and smoother surface morphology (b); powders obtained after 15 (c), 30 (d), 60 (e), and 240 (f) min of milling

or elongated. The morphology clearly reflected the ribbon's original columnar structure. Fragments with flat fracture surfaces and sharp edges were visible, indicating the material's brittle character. After 30 minutes (Fig. 1d), fragmentation was continued, resulting in a reduction of the average particle size and an increase in particle number. An increase in morphological irregularity was also observed, along with the presence of finer fragments between larger particles. At the same time, elongated particles remained, indicating that the fragmentation process was not yet completed and that the fracture mechanism still retained features inherited from the initial microstructure. Extending the milling time to 60 minutes (Fig. 1e) resulted in a further increase in fragmentation and the formation of a significant number of fine particles. The powder morphology became more homogeneous in particle shape; however, larger fragments remained. Particle clusters were also observed, suggesting the initiation of secondary agglomeration processes. After 240 minutes (Fig. 1f), a significant change in powder microstructure was observed. A large number of fine particles of similar size (on the order of several micrometres) were present, forming extensive clusters and agglomerates. Individual particles remained clearly distinguishable, indicating an advanced degree of material fragmentation. At the same time, pronounced secondary agglomeration processes were evident, leading to the formation of agglomerates with larger effective sizes.

3.2. Chemical and phase composition

Milling time affected the chemical composition of the powders, as shown by the changes in the content of individual elements in Fig. 2. For nickel, the measured content in the as-spun ribbon was 51.85 at.%, slightly higher than the nominal value. After 15 minutes, its content was increased to approximately 51.8 at.%. Consequently, as milling time increased, a gradual increase in nickel content was observed, reaching 52.4 at.% after 30 min and 52.8 at.% after 60 min. For the longest time (240 min), its concentration was approximately 52.9 at.%. It should be noted that in the milling time range of 60–240 min, the change in nickel content was only about 0.1 at.%, indicating that milling time had no significant effect on its concentration in the alloy. The observed variations are low, indicating a relatively stable content. These minor fluctuations may result from composition normalisation effects associated with changes in the relative content of other elements, particularly gallium.

For manganese, the measured content in the ribbon was approximately 28.7 at.%, exceeding the nominal value. After 15 minutes, the manganese content increased to 29.5 at.%. With further milling (30 min and 60 min), its content remained at a similar level, reaching 29.8 at.% and 29.7 at.%, respectively. For the longest time (240 min), the manganese content was 29.7 at.%, indicating a practically constant level in the range of 60-240 min. The observed trend shows an initial increase in manganese content followed by stabilisation. This trend does not reflect actual enrichment in manganese but is rather a relative effect associated with changes in gallium content in the alloy.

A different behaviour was observed for gallium. In the ribbon, its content was 19.4 at.% – lower than the nominal value. After the onset of milling, the gallium content decreased markedly to 18.7 at.% after 15 min. With increasing milling time, a systematic decrease in gallium content was observed, reaching 17.8 at.% after 30 min and 17.5 at.% after 60 min. After 240 minutes, the gallium content reached the same value as previously, 17.5 at.% proving its stabilisation in the range of 60-240 min. This behaviour suggests a gradual loss of gallium during milling. Effect may be related to its relatively low melting point compared to the other alloying elements. Under conditions of intensive mechanical milling, the supplied energy

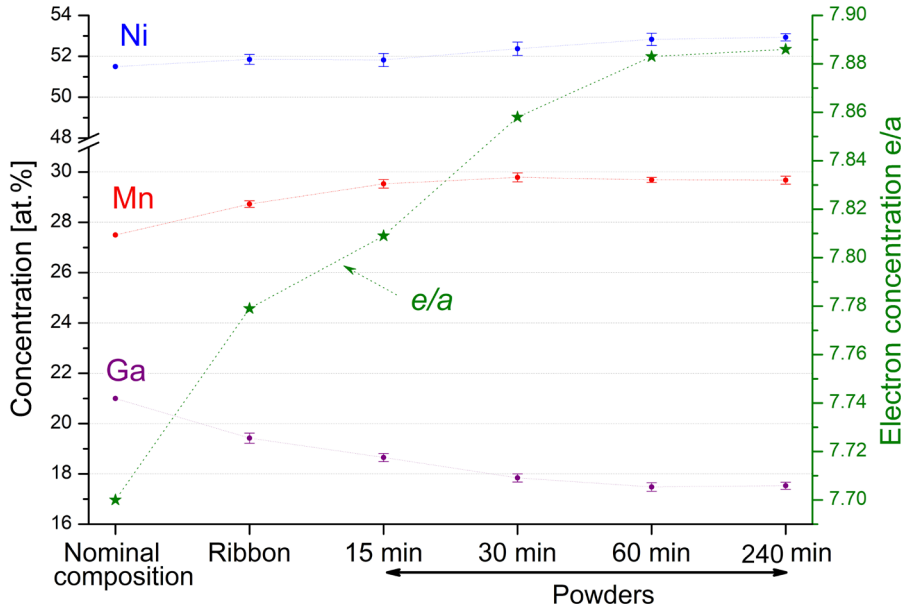

Fig. 2. Chemical composition and valence electron concentration of the Ni–Mn–Ga alloy: nominal composition and values measured for the ribbon and milled powders

and local temperature increases may lead to partial evaporation or oxidation of gallium.

The changes in chemical composition resulted in a variation in the valence electron concentration – *e*/*a* (Fig. 2). With increasing milling time, a systematic increase in the *e*/*a* parameter was observed, from 7.78 for the ribbon to 7.81 after 15 minutes, 7.86 after 30 minutes, and 7.88 after 60 minutes of milling. For the longest milling time (240 minutes), the e/a value reached 7.89. It showed that, over the range of 60-240 minutes, this parameter is almost constant. Such a trend is associated with increased Ni and Mn concentrations, accompanied by a decrease in Ga content. Nickel and manganese provide the dominant contribution to the valence electron concentration. The relationship between the martensitic transformation temperature and the *e*/*a* parameter is well established for Ni–Mn–Ga alloys. An increase in *e*/*a*, resulting from higher Ni and Mn content at the expense of Ga, stabilises the martensitic phase and shifts the transformation temperatures toward higher values [18,19]. These results are supported by the phase composition determined by X-ray diffraction.

Fig. 3 presents the diffraction patterns of the initial ribbon and the milled powders. First, the analysis was performed for the as-spun ribbon. The diffraction pattern showed only peaks characteristic of the parent phase with an $L2_1$ structure, considered the highest degree of ordering in Ni–Mn–Ga alloys. To interpret possible changes in the ordering state of the parent phase, it is useful to recall the characteristic diffraction features of A2, B2, and $L2_1$ structures in Ni–Mn–Ga alloys. The order-disorder transformation in this group of alloys is related to changes in the occupancy of lattice sites by alloying elements. In the case of the fully disordered A2-type bcc structure, atoms occupy lattice positions randomly, and only fundamental reflections are observed. Partial ordering leads to the B2-type structure, in which Ni atoms occupy one sublattice, while Mn and Ga atoms share the other sublattice. This ordering gives rise to superlattice reflections such as (001)B2. The highest degree of ordering corresponds to the $L2_1$ structure, in which Mn, Ga, and Ni atoms occupy well-defined lattice sites in an enlarged unit cell with a parameter of approximately 5.8 Å. In this case, additional superlattice reflections appear, among which the (111) $L2_1$ reflection is characteristic of the $L2_1$ orders. This structural sequence was used solely as a reference to assess whether milling caused disordering of the parent phase.

Milling for 15 min initiated the martensitic transformation, induced by stresses generated by the vibrating milling ball. With increasing milling time, the intensity of diffraction lines characteristic of the $L2_1$ structure systematically decreased. At the same time, the first low-intensity reflections characteristic of 14M martensite appeared. After 30 min of milling, the parent phase remained. However, the martensite fraction increased, confirming the transformation's progress. Fig. 3b compares the low-angle regions of the diffraction patterns. It confirms the gradual disappearance of reflections belonging to the parent $L2_1$ phase, without evidence of a transition to the B2-type structure. It suggests a direct transition from the parent $L2_1$ phase to 14M martensite. It should be noted that, for alloys with an electron concentration e/a close to 8, the occurrence of non-modulated NM martensite is also possible. However, the performed simulations and structural fitting confirmed that the observed diffraction lines are mainly consistent with 14M martensite. A visible effect of this transformation is the appearance of the (111)14M diffraction line in place of the (111)$L2_1$ line, shifted by approximately 0.1° 2θ toward higher diffraction angles. After 60 minutes, the diffraction pattern was dominated by reflections from the martensitic phase, while the fraction of the $L2_1$ phase decreased, leading to the disappearance of its characteristic peaks.

After 240 minutes, all observed diffraction peaks were attributed to the 14M martensite, confirming the complete transformation of the parent phase. At the same time, the intensity

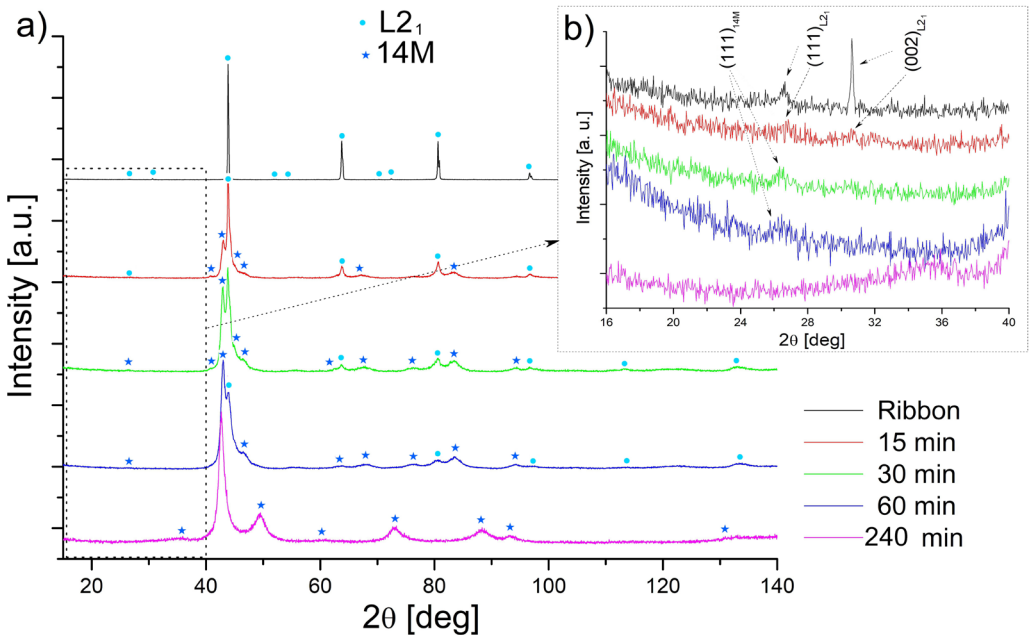

Fig. 3. X-ray diffraction patterns of the ribbon and milled powders (a) and enlarged low-angle region (15-40° 2θ) (b)

distribution of the reflections differed slightly from that of the samples milled for 30 and 60 minutes. These changes can be associated with progressive grain refinement of the powder, particularly pronounced after 240 minutes of milling, as discussed in the following section. This effect may influence the degree of texture and the preferred grain orientation in the sample holder, leading to the appearance of martensitic reflections that were previously undetected.

The structural evolution of the alloy triggered by the milling time elongation indicates a transition from the highly ordered $L2_1$ phase to the 14M martensite. The observed transformation results from both mechanical stresses generated during milling and changes in chemical composition, which alter the valence-electron concentration. An increase in e/a shifts the martensitic transformation temperature toward higher values. As a result, measurements performed at room temperature indicate that the material, after prolonged milling, is in the martensitic state. Additionally, internal stresses generated during milling promote the martensitic transformation, reinforcing the effect of chemical composition changes.

3.3. Effect of milling time on particle and crystallite size

Fig. 4a presents the particle size distributions of powders obtained after different milling times. In the particle-size analysis, Q3 represents the cumulative volume distribution, while dQ3 denotes the volume-based differential distribution, expressed as the volume fraction of particles in individual size classes.

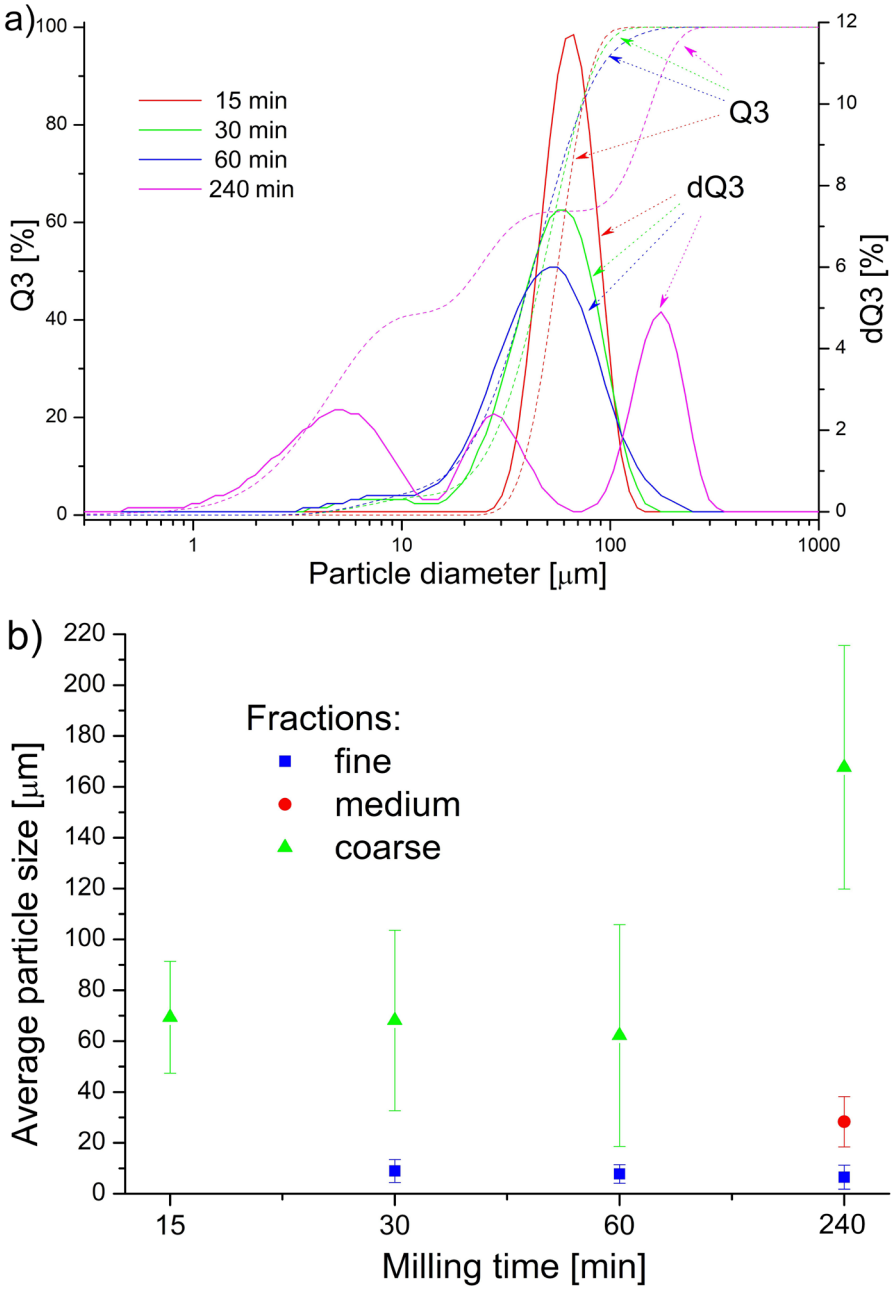

Fig. 4. Particle size distributions (Q3) of milled powders (a) and the variation of average particle size with milling time (b)

Based on these results, parameters describing the distributions were determined. The most important parameter for characterising the comminution process is the particle size. It should be emphasised that the values of D(4,3), D50, and other statistical parameters refer to the main particle fraction corresponding to the dominant peak in the differential dQ3 curves. SEM observations (Fig. 1) indicate that in the initial stage of milling, the particles undergo intensive fragmentation. This is confirmed by the volume-weighted mean diameter D(4,3), which decreases from 63 μm after 15 min to about 52 μm after 60 min. A similar trend is observed for the median diameter (D50), which decreases from 61 μm to 46 μm. This indicates a shift of the main part of the distribution toward smaller particle sizes.

Analysis of the variation coefficient (CV) shows that changes in powder homogeneity with milling time are non-monotonic. After 15 minutes of milling, the high CV value (90.0%) reveals a very broad particle size distribution, typical of the initial stage of the process. Increasing the milling time to 30 minutes leads to a clear narrowing of the distribution (CV = 46.3%), indicating improved powder homogeneity. Extending the milling time to 60 minutes increases the CV (61.0%), proving greater size dispersion. This trend is confirmed by the standard deviation (σ), which decreases from 57 μm (15 min) to 25 μm (30 min), and then increases to 32 μm after 60 minutes. The increase in σ at this stage reveals the coexistence of particles of different sizes, consistent with the presence of both fine particles and larger agglomerates.

At the longest milling time (240 min), a distinct change in process behaviour is observed. The volume-weighted mean diameter D(4,3) increases to 70.5 μm, indicating a reversal of the earlier trend of particle size reduction. At the same time, the median (D50) reaches approximately 25.1 μm. It confirms the presence of fine fraction particles. The simultaneous, very high increase in the coefficient of variation (CV = 113.2%) and standard deviation ($\sigma \approx 80$ μm) is a consequence of the formation of an extremely broad particle size distribution. In addition, the high mode value (~166.07 μm) and positive skewness (1.147) indicate a significant contribution of large particles. Together with the large span (7.514), it proves the coexistence of very fine particles and large agglomerates..

The analysis of parameters such as D(4,3), D50, and CV presented above primarily reflects the dominant particle fraction corresponding to the main peak in the differential dQ3 curves. While this approach is sufficient for practical powder characterisation, it does not fully capture the complexity of the fragmentation mechanisms. In particular, it does not account for additional particle populations, which become evident in a more detailed analysis of the particle size distributions.

Fig. 4b shows the dependence of mean particle size on milling time. The average particle diameters were determined by fitting lognormal function to the experimental particle size distributions. The quality of the peak fitting was confirmed by high values of the coefficient (R^2), ranging from 0.97 to 0.99.

For the powder milled for 30 minutes, in addition to the dominant fraction with a mean particle size of 68.2 μm, a population of particles with a diameter of about 8.9 μm is also present. However, the peak analysis refers to the volume-based particle size distribution and indicates that this fine fraction contributes only 0.99%, while the coarse fraction accounts for approximately 99.01% of the total distribution. A similar situation was observed in powders milled for 60 minutes, where, in addition to the coarse fraction (~62 μm), a fine fraction with a diameter of about 7.8 μm was identified, whose contribution is practically negligible (0.01%). Thus, within this milling time range, the volume-based distribution remains dominated by a single population of larger particles, accounting for approximately 99% of the total distribution.

A distinct change in the character of the distribution occurs only after 240 minutes of milling, when three separated peaks appear in the derivative dQ3 curve. It proved the formation of three particle fractions: fine, intermediate, and coarse. The fine fraction, with a mean particle size of approximately 6.5 μm, accounts for about 0.34%. The intermediate fraction, with a diameter of about 28.3 μm, accounts for approximately 2%. In contrast, the coarse fraction, with a mean particle size of about 167.7 μm, remains dominant, accounting for about 97.7% of the total distribution.

The presented particle size analysis is at the micrometre scale and reflects the actual sizes of particles and their agglomerates. These results are in good agreement with X-ray diffraction measurements, which allow evaluation of changes in the crystal lattice by determining crystallite size and lattice strain. From the measurement, the full width at half maximum (FWHM) of the diffraction peaks was determined. Subsequently, the Williamson-Hall method was applied to evaluate the effect of milling on these parameters quantitatively. This method enables separation of the contributions of crystallite size and microstrain to peak broadening [17]. In contrast to the Scherrer method [20], which considers only crystallite size, the Williamson-Hall approach provides a more comprehensive interpretation of the mechanisms responsible for peak broadening.

The results confirmed that increasing milling time decreases crystallite size (Fig. 5a). In the initial sample (ribbon), only the parent $L2_1$ phase was present. The calculated crystallite size was 107.5 ± 13 nm. This value lies at the limit of applicability of the Williamson-Hall method and is associated with increased uncertainty. However, it provides an important reference point for comparison with milled material. For the parent $L2_1$ phase, a systematic decrease in crystallite size was observed with increasing milling time. The crystallite size decreased to 55.0 ± 0.3 nm after 15 min, 49.8 ± 5.9 nm after 30 min, and 39.2 ± 0.8 nm after 60 min. The observed reduction in crystallite size results from intensive plastic deformation. Structural defects introduced during the process, such as dislocations and local lattice distortions, increase the heterogeneity of the crystal structure and reduce the effective size of coherently scattering domains.

External stresses generated during milling not only reduce crystallite size but also promote the induction of the martensitic transformation, leading to the formation of 14M martensite. This phase was not present in the as-spun ribbon and appears only in the milled materials. The average crystallite size in martensite

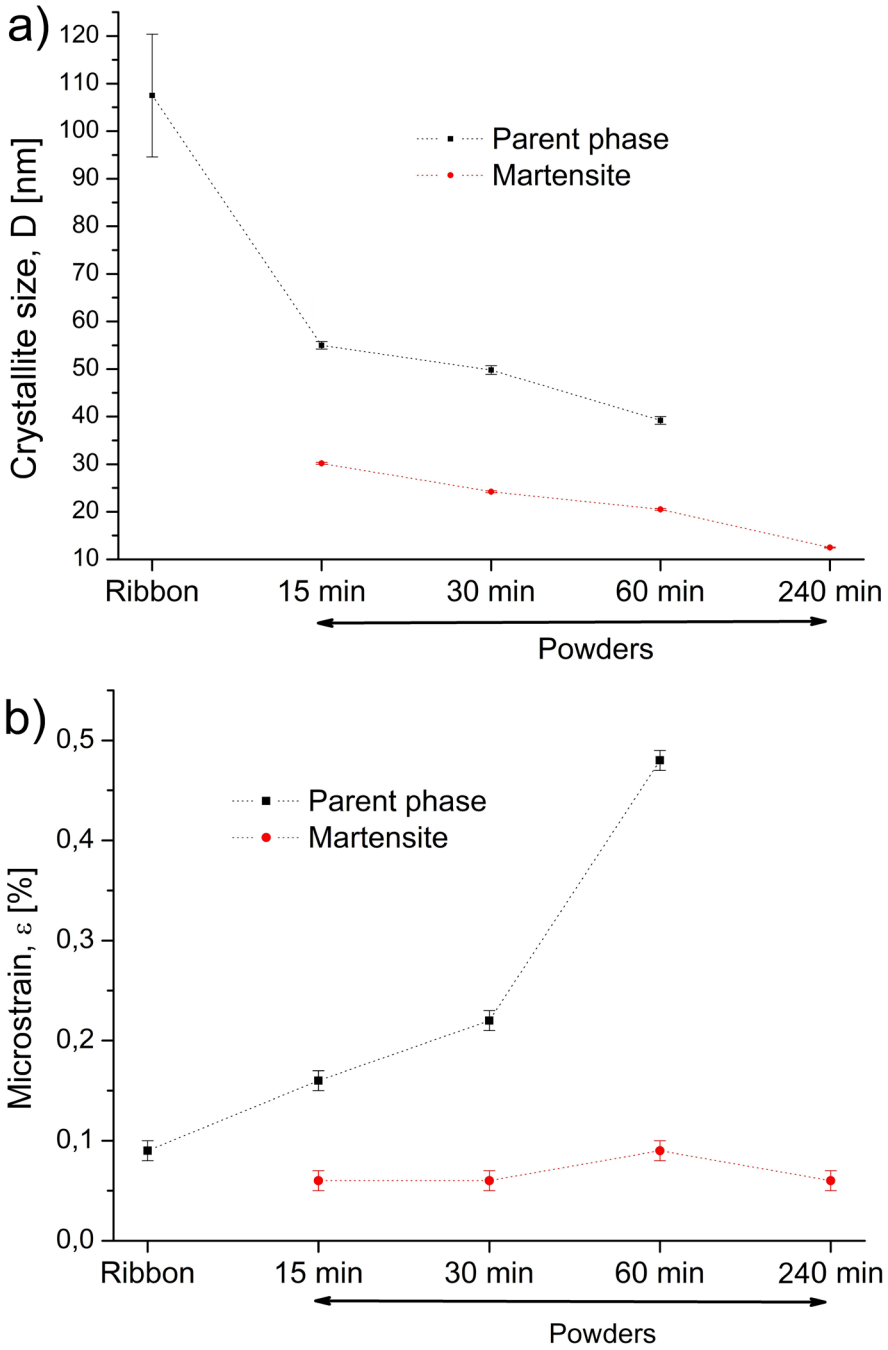

Fig. 5. Crystallite size (a) and microstrain (b) for the as-spun ribbon and milled powders

is significantly smaller than that determined for the parent phase (Fig. 5a). It decreases from 30.2 ± 0.1 nm (15 minutes), through 24.2 ± 0.1 nm (30 minutes) and 20.5 ± 0.1 nm after 60 minutes, to 12.5 ± 0.1 nm after 240 minutes. It is noteworthy that for all analysed milling times, the standard deviation of the crystallite size of 14M martensite remains very low (±0.1 nm). It indicates a relatively narrow crystallite size distribution and high structural uniformity. In contrast, the parent phase exhibits a different trend, with standard deviation values of 0.3 nm (15 min), 5.9 nm (30 min), and 0.8 nm (60 min), indicating greater variation in crystallite size.

The analysis of lattice strain reveals a phase-dependent evolution (Fig. 5b). In the initial ribbon, the lattice strain in the $L2_1$ phase was 0.09 ± 0.01%. Although the ribbon was produced by rapid solidification during melt spinning, this value remains relatively low. Mechanical milling introduces internal stresses into the material, which results in a clear increase in lattice strain with increasing milling time. The strain reaches 0.16 ± 0.01%, 0.22 ± 0.01%, and 0.48 ± 0.01% after 15, 30, and 60 min of milling, respectively. It can be attributed to the accumulation of structural defects, such as dislocations and local lattice distortions, generated during the intensified milling process.

A different behaviour was observed for martensite. In this phase, a natural broadening of diffraction peaks occurs due to the presence of martensitic plates and their self-accommodation. The effect of milling on the strain state in this phase is limited and

becomes noticeable only after 60 minutes. For the powder milled for 15 minutes, the lattice strain was 0.09 ± 0.01%, while for longer milling times it decreased to 0.06 ± 0.01%. The low strain values indicate a limited tendency for martensite to accumulate deformation, which is related to its characteristic deformation mechanisms, such as twinning and/or variant reorientation. Also, the low standard deviation values (±0.01%) prove a high uniformity of the strain distribution within the analysed material.

4. Conclusions

1. Extension of milling time affects the chemical composition of the alloy selectively, leading primarily to a decrease in gallium content. In contrast, the nickel and manganese contents remain relatively stable (particularly in the 60-240 min range). The compositional changes are of low amplitude, not exceeding ~2 at.% with respect to the nominal composition and about 1 at.% relative to the initial material (as-spun ribbon). Despite their limited magnitude, these changes result in a systematic increase in the valence-electron concentration (e/a), which stabilises at the final stage of the process.
2. The increase in e/a, together with stresses generated during milling, promotes the induction of the martensitic transformation, resulting in a transition from the high ordered $L2_1$ parent phase to a structure dominated by 14M martensite, without evidence of an intermediate decrease in the degree of ordering toward the B2 structure.
3. Milling leads to a reduction in both particle and crystallite size, although these changes occur at different scales. Powder particles remain in the micrometer range and exhibit an agglomerated character, while crystallite size is reduced to the nanometer scale. Increasing milling time initially results in intensive fragmentation and a decrease in mean particle size, whereas at longer times (240 min), secondary agglomeration becomes dominant. As a result, an increase in mean particle diameter and a broadening of the particle size distribution were observed.
4. The evolution of lattice strain in the milled powders is phase-dependent. In the parent $L2_1$ phase, a clear increase in lattice strain was observed with increasing milling time, from approximately 0.09% to 0.48%. In contrast, in the 14M martensite phase, lattice strain remains low (~0.1%) and shows lower dependence on milling time.

REFERENCES

[1] P.J. Webster, K.R.A. Ziebeck, S.L. Town, M.S. Peak, Phil. Mag. B, **49**, 295-310 (1984).

[2] K. Ullakko, J.K. Huang, C. Kantner, R.C. O'Handley, V.V. Kokorin, Appl. Phys. Lett. **69**, 1966-1968 (1996).

[3] A. Sozinov, A.A. Likhachev, N. Lanska, K. Ullakko, Appl. Phys. Lett. **80**, 1746-1748 (2002).

[4] K. Otsuka, C.M. Wayman, Shape Memory Materials, Cambridge University Press, Cambridge 1998.

[5] K. Tsuchiya, A. Tsutsumi, N. Ina, M. Umemoto, H. Ohtsuka, Trans. Mater. Res. Soc. Japan, **28**, 269-270 (2003).

[6] S. Singh, V. Petricek, P. Rajput, A.H. Hill, E. Suard, S.R. Barman, D. Pandey, J. Magn. Magn. Mater. **323**, 574-579 (2011).

[7] J. Pons, R. Santamarta, V.A. Chernenko, E. Cesari, Mater. Sci. Eng.A **273-275**, 315-319 (1999).

[8] V. Recarte, J.I. Pérez-Landazábal, C. Gomez-Polo, C. Seguí, E. Cesari, P. Ochin, Mater. Sci. Eng. A **438-440**, 927-930 (2006).

[9] T. Goryczka, J. Lelatko, B. Górka-Kostrubiec, P. Ochin, H. Morawiec, The European Physical Journal Special Topics **158**, 131-136 (2008).

[10] A. Wójcik, R. Chulist, P. Czaja, M. Kowalczyk, P. Zackiewicz, N. Schell, W. Maziarz, Acta Mater. **219**, 117237 (2021).

[11] K. Vallal Peruman, M. Mahendran, Pure Appl. Chem. **83**, 2071-2077 (2011).

[12] B. Tian, F. Chen, Y.X. Tong, L. Li, Y.F. Zheng, Y. Liu, Q.Z. Li, J. Alloys Compd. **509**, 4563-4568 (2011).

[13] B. Tian, F. Chen, Y.X. Tong, L. Li, Y.F. Zheng, Y. Liu, Q.Z. Li, J. Mater. Eng. Perform. **21**, 2530-2534 (2012).

[14] P. Ochin, A.V. Gilchuk, G.E. Monastyrsky, Y. Koval, A.A. Shcherba, S.N. Zaharchenko, Mater. Sci. Forum **738-739**, 451-455 (2013)

[15] B.A. Hunter, Comm. Powder Diffr. **20**, 21 (1998).

[16] L. Zhou, A. Giri, K. Cho, H. Heinrich, B.S. Majumdar, Y. Sohn, Metall. Mater. Trans. E **1E**, 239-246 (2014).

[17] G.K. Williamson, W.H. Hall, Acta Metall. **1**, 22-31 (1953). DOI: https://doi.org/10.1016/0001-6160(53)90006-6

[18] V.A. Chernenko, Scripta Mater. **40**, 523-527 (1999). DOI: https://doi.org/10.1016/S1359-6462(98)00494-1

[19] J. Pons, R. Santamarta, E. Cesari, Acta Mater. **48**, 3027-3038 (2000). DOI: 10.1016/S1359-6454(00)00180-3

[20] A.L. Patterson, Phys. Rev. **56**, 978-982 (1939). DOI: https://doi.org/10.1103/PhysRev.56.978